International Journal of Heat and Mass Transfer 61 (2013) 254–265

Contents lists available at SciVerse ScienceDirect

International Journal of Heat and Mass Transfer

journal homepage: www.elsevier.com/locate/ijhmt

Variational formulation on Joule heating in combined electroosmotic and pressure driven microflows

Arman Sadeghi [a], Mohammad Hassan Saidi [a], Zakariya Waezi [b], Suman Chakraborty [c,*]

[a] Center of Excellence in Energy Conversion (CEEC), School of Mechanical Engineering, Sharif University of Technology, P.O. Box 11155-9567, Tehran, Iran
[b] Department of Civil Engineering, Sharif University of Technology, Tehran, Iran
[c] Department of Mechanical Engineering, Indian Institute of Technology, Kharagpur 721302, India

ARTICLE INFO

Article history:
Received 18 October 2012
Received in revised form 18 December 2012
Accepted 26 January 2013

Keywords:
Electroosmotic flow
Microchannel
Joule heating
EDL

ABSTRACT

The present study attempts to analyze the extended Graetz problem in combined electroosmotic and pressure driven flows in rectangular microchannels, by employing a variational formulation. Both the Joule heating and axial conduction effects are taken into consideration. Since assuming a uniform inlet temperature profile is not consistent with the existence of these effects, a step change in wall temperature is considered to represent physically conceivable thermal entrance conditions. The method of analysis considered here is primarily analytical, in which series solutions are presented for the electrical potential, velocity, and temperature. For general treatment of the eigenvalue problem associated with the solution of the thermal field, an approximate solution methodology based on the variational calculus is employed. An analytical solution is also presented by considering thin electrical double layer limits. The results reveal non-monotonic behaviors of the Nusselt number such as the occurrence of singularities in the local Nusselt number values when the fluid is being heated from the wall. Moreover, the effect of increasing the channel aspect ratio is found to be increasing both the temperature difference between the wall and the bulk flow and the Nusselt number. In addition, higher wall heat fluxes are obtained in the entrance region by increasing the Peclet number.

1. Introduction

With the advent of microfluidics, electroosmosis has featured as an important mechanism for flow generation in modern microscale laboratories, capable of performing medical diagnoses, known as lab-on-a-chip. Electroosmotic micropumps have many advantages over the other types of micropumps. For example, unlike the classical pressure driven micropumps containing moving components that are complicated to design and fabricate, the electroosmotic pumps have no moving parts and are more elegantly integrable with on-chip electrical circuitry. Moreover, these pumps are bidirectional and capable of generating constant and pulse free flows with flow rates well suited to microsystems [1].

The fundamental origin of electroosmotic transport lies in the fact that when a surface is brought into contact with an electrolyte solution, it may assume a net charge. Due to the electroneutrality principle, the liquid takes on an opposite charge in the electric double layer (EDL) near the surface. The electric double layer, shown schematically in Fig. 1, contains an immobile inner layer and an outer diffuse layer [2]. If an electric field is applied tangentially along the surface, a force will be exerted on the ions within the mobile diffuse electric layer resulting in their motion [3]. Owing to viscous drag, the liquid is drawn by the ions and therefore flows tangent to the surface. Such a fluid flow, which was explored about two centuries ago [4], is referred to as electroosmotic flow.

The study of electroosmotic flow in microchannels can be traced to 1960s. One of the first attempts in this context was carried out by Burgreen and Nakache [5] who theoretically analyzed the electrokinetic flow in ultrafine capillary slits. Rice and Whitehead [6] investigated the fully developed electroosmotic flow in a narrow cylindrical capillary for low zeta potentials, using the Debye–Hückel linearization. Subsequently, Levine et al. [7] extended the Rice and Whitehead's work to high zeta potentials by means of an approximation method. More recently, Kang et al. [8] analytically investigated electroosmotic flow through an annulus under the situation when the two cylindrical walls carry high zeta potentials. Analytical solutions for fully developed electroosmotic flow in rectangular and semicircular microchannels were presented by Yang [9] and Wang et al. [10], respectively.

Unlike the hydrodynamic features, the study of the thermal features of electroosmosis is recent. The majority of the research works performed in this area deals with Joule heating effect, a phenomenon which arises from the applied electric field and fluid

* Corresponding author.
E-mail addresses: armansadeghi@mech.sharif.edu (A. Sadeghi), saman@sharif.edu (M.H. Saidi), waezi@mehr.sharif.edu (Z. Waezi), suman@mech.iitkgp.ernet.in (S. Chakraborty).

0017-9310/$ - see front matter © 2013 Elsevier Ltd. All rights reserved.
http://dx.doi.org/10.1016/j.ijheatmasstransfer.2013.01.065

Nomenclature

$\mathbb{A}$	channel area (m^2)
c_p	specific heat at constant pressure ($kJkg^{-1}K^{-1}$)
D_h	hydraulic diameter of channel [$=4HW/(H+W)$]
e	proton charge (C)
$\mathbf{E}$	electric field (Vm^{-1})
E_x	electric field in the axial direction (Vm^{-1})
f	basis function
$\mathbf{F}$	body force vector (Nm^{-3})
$\mathbb{F}_n$	eigenfunction, $x \leqslant 0$
$\mathbb{G}_n$	eigenfunction, $x \geqslant 0$
h	heat transfer coefficient ($Wm^{-2}K^{-1}$)
H	half channel height (m)
$\mathbf{I}$	identity matrix
k	thermal conductivity ($Wm^{-1}K^{-1}$)
k_B	Boltzmann constant (JK^{-1})
$\mathbb{n}$	outward normal direction to the wall (m)
n_0	ion density at neutral conditions (m^{-3})
Nu	Nusselt number [$=hD_h/k$]
p	pressure (Pa)
$\mathbb{P}$	duct boundary (m)
Pe	Peclet number [$=\rho c_p u_{HS} H/k$]
s	volumetric heat generation due to Joule heating (Wm^{-3})
S	dimensionless Joule heating parameter [$=E_x^2H^2/k\sigma_0(T_0-T_w)$]
t	time (s)
T_w	wall temperature in downstream region (K)
T_0	wall temperature in upstream region (K)
u	axial velocity (ms^{-1})
$\mathbf{u}$	velocity vector (ms^{-1})
u_{HS}	Helmholtz–Smoluchowski velocity [$=-\varepsilon\zeta E_x/\mu$]
u_{PD}	pressure driven velocity [$=-H^2(\partial p/\partial x)/2\mu$]
W	half channel width (m)
x,y,z	coordinates (m)
$\mathcal{Z}$	valence number of ions in solution

Greek symbols

α	channel aspect ratio [$=W/H$]
β_n	eigenvalue, $x \geqslant 0$
Γ	velocity scale ratio [$=u_{PD}/u_{HS}$]
ε	fluid permittivity ($CV^{-1}m^{-1}$)
ζ	zeta potential (V)
θ	dimensionless temperature [$=(T-T_w)/(T_0-T_w)$]
K	dimensionless Debye–Hückel parameter [$=H/\lambda_D$]
λ_D	Debye length (m)
λ_n	eigenvalue, $x \leqslant 0$
μ	dynamic viscosity ($kgm^{-1}s^{-1}$)
ρ	fluid density (kgm^{-3})
ρ_e	net electric charge density (Cm^{-3})
σ_0	electrical resistivity at neutral conditions [Ωm]
$\boldsymbol{\tau}$	stress tensor (Pa)
ϕ	electrostatic potential (V)
Φ	externally imposed electrostatic potential (V)
ψ	EDL potential (V)

Subscripts

av	average
b	bulk
p	particular solution
1	$x \leqslant 0$
2	$x \geqslant 0$

Superscript

$*$	dimensionless variable

electrical resistivity. The temperature rise due to the Joule heating can be detrimental for the samples being considered in lab-on-a-chip devices. Hence, studying the thermal aspects of electroosmosis is vital in design and active control of these devices. Besides, although, primarily because of the Joule heating effects, electroosmosis is not usually employed for heat removal purposes, possible potentials towards fulfilling such objectives appear to be immense [11,12].

Pioneering studies on the heat transfer characteristics of electroosmosis were performed by Maynes and coworkers [13–15]. Their investigations dealt with the thermally fully developed electroosmotic flow at small [13] and high [14] zeta potentials as well as viscous heating effects on the thermal transport characteristics [15]. Some other related works have been reported on the thermal transport in combined electroosmotic and pressure driven flow. Such a combined flow usually arises when a pressure driven pumping system is added to the electroosmotic pumping systems in order to reduce the Joule heating effects. Chakraborty [16] obtained analytical solutions of Nusselt number for thermally fully developed flow in microtubes under a combined action of electroosmotic forces and imposed pressure gradients. In two separate studies, Sadeghi and Saidi [17] and Chakraborty et al. [18] considered viscous dissipation effects on the thermal features of combined electroosmotic and pressure driven flow in a parallel plate microchannel. Garai and Chakraborty [19] presented a theoretical analysis for fully developed convective heat transfer in two immiscible fluid layers confined within parallel plate microchannels subject to combined effects of axial pressure gradients and imposed

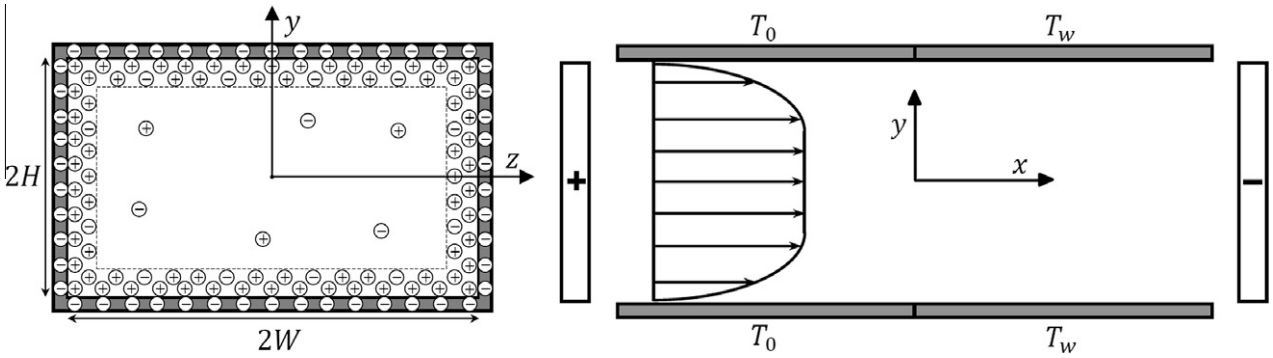

Fig. 1. Schematic of the physical problem along with the coordinate system; EDLs are the regions between the dashed lines and the channel walls.

electrical fields. In a recent study, Sadeghi et al. [20] reported the results of a numerical investigation on temperature dependent effects on mixed electroosmotic and pressure driven flows. The most recent work of this research group deals with both analytical and numerical investigation of the hydrodynamic and thermal characteristics of mixed flow in a microannulus [21].

The problem of hydrodynamically fully developed and thermally developing flow in a channel, with the assumptions of constant fluid properties and negligible energy dissipation and streamwise conduction effects is known as the Graetz problem [22,23]. Since its original solution, the Graetz problem has served as an archetypal convective heat transfer problem both from a process modeling and an educational point of view. The classical Graetz problem assumes a uniform inlet temperature, shown here as T_0. However, in microflows, because of the axial conduction effects, the fluid temperature is affected by the wall temperature, shown here as T_w, even before entering the channel [24–29]. In this case, all can be said is that the fluid temperature is uniform at T_0 away from the entrance. Therefore, the solution domain should be extended to include the upstream region and a wall temperature should be considered for this section. The assumed temperature should be consistent with the condition that the fluid temperature away from the entrance is T_0 which turns out in a wall temperature of T_0. The wall temperature therefore should contain a step change from T_0 to T_w at the channel inlet to physically imitate the thermal entrance condition. The previous explanation is for the case without internal heating; however, for extending the Graetz problem to electroosmotic flow, one also should take into account the temperature distribution caused by the Joule heating.

There are some research works which extend the Graetz problem to electroosmotic flow in microchannels. Nevertheless, the majority of these studies assume a uniform inlet temperature. Dutta and coworkers [30–32] extended the Graetz problem to electroosmotic and also mixed electroosmotic and pressure driven flow through two dimensional straight microchannels for both classical boundary conditions of constant wall temperature and constant wall heat flux. Broderick et al. [33] numerically analyzed the thermally developing electroosmotic flow in circular microtubes for both constant wall heat flux and constant wall temperature boundary conditions. Iverson et al. [34] developed analytical solutions for thermally developing electroosmotic flow with vanishing Debye length in rectangular microchannels. All the above mentioned papers assume a uniform inlet temperature. To the authors' best knowledge, the only research works in this context considering a physically meaningful thermal condition at the channel entrance have been performed by Sharma and Chakraborty [35], Dey et al. [36,37], and Sadeghi et al. [38]. These studies are dealing with mixed flow with vanishing [35] and finite [36–38] Debye lengths in a slit microchannel.

In most lab-on-a-chip systems, the cross section of microchannels made by modern micromachining technology is close to a rectangular shape [39,40]. However, in studying the heat transfer features of electroosmosis, the rectangle geometry has received much less attention compared with the circular and parallel plate microchannels. As mentioned previously, the only study dealing with a thermally developing electroosmotic flow in rectangular microchannels, performed by Iverson et al. [34], assumes a uniform inlet temperature. Furthermore, the authors represented the effect of EDL by the Helmholtz–Smoluchowski velocity which limits their analysis to a purely electroosmotic flow with the channel height to Debye length ratio of above 100.

The aim of the present work is to theoretically investigate the thermally developing combined electroosmotic and pressure driven flow in a rectangular microchannel by considering the actual variations of the velocity within EDL and applying a step change to the wall temperature. The problem is considered in two semi-infinite regions of the channel, i.e., upstream in which $x \leq 0$ and downstream in which $x \geqslant 0$ and the solutions of the two regions are then matched at $x = 0$. Analytical solutions in the form of infinite series are obtained for the electrical potential, velocity, and temperature. For general treatment of the eigenvalue problem associated with the thermal solution, variational calculus, having been found to be more accurate as compared with similar methods [28], is employed. An analytical solution is also presented by assuming a uniform velocity profile which is valid for a purely electroosmotic flow with vanishing Debye length. Finally, a detailed discussion is performed on the obtained results by physical interpretation of the trends.

2. Problem formulation

2.1. Problem definition

Consideration is given to combined electroosmotic and pressure driven flow through a long rectangular microchannel with dimensions given in Fig. 1. The flow is assumed to be hydrodynamically fully developed. The wall temperature is the constant T_0 when $x < 0$ and it is the constant T_w, when $x > 0$. In the analysis, the following assumptions are considered:

- Thermophysical properties are constant in the whole domain including EDL.
- The zeta potential is constant.
- Liquid contains an ideal solution of fully dissociated symmetric salt.
- Wall potentials are considered low enough for Debye–Hückel linearization to be valid.
- In calculating the charge density, it is assumed that the temperature variation over the entire channel is negligible compared with the absolute temperature. Therefore, the charge density field is calculated on the basis of an average temperature.

2.2. Electrical potential distribution

The electrostatic potential, ϕ, at any point in the channel will be described by superposition of the externally applied potential, Φ, along the channel axis, and the double layer potential, ψ. Using the coordinate system shown in Fig. 1, at the fully developed conditions $\psi = \psi(y,z)$, so

$$\phi(x,y,z) = \Phi(x) + \psi(y,z) \tag{1}$$

The electrostatic potential is related to the local net charge density, ρ_e, at certain point in the solution by the Poisson equation:

$$\nabla^2\phi = -\frac{\rho_e}{\varepsilon} \tag{2}$$

where ε is the permittivity constant of the solution. In general, the Nernst–Planck equations should be used to relate the electric charge density to the electrostatic potential. However, at the fully developed conditions, the spatial distribution of the electric charge density is described by the Boltzmann equation, in spite of the fact that it assumes the thermodynamic equilibrium [41]. This is due to the fact that, at the fully developed conditions, the velocity vector and the ion concentration gradient are perpendicular to each other. Using the Boltzmann distribution, the electric charge density for an ideal symmetric electrolyte of valence $\mathcal{Z}$ is given by [2]

$$\rho_e = -2n_0 e\mathcal{Z}\sinh\left(\frac{e\mathcal{Z}\psi}{k_B T}\right) \tag{3}$$

where n_0 is the ion density at neutral conditions, e is the proton charge, k_B is the Boltzmann constant and T is the absolute temperature. Yang et al. [42] have shown that the effect of temperature on

the potential distribution is negligible, using extensive numerical simulations. Therefore, the potential field and the charge density may be calculated on the basis of the average temperature, T_{av}. For a constant voltage gradient in the x -direction, Eq. (2) becomes

$$\frac{\partial^2\psi}{\partial y^2}+\frac{\partial^2\psi}{\partial z^2}=\frac{2n_0e\mathcal{Z}}{\varepsilon}\sinh\left(\frac{e\mathcal{Z}\psi}{k_BT_{av}}\right) \tag{4}$$

and in the dimensionless form

$$\frac{\partial^2\psi^*}{\partial y^{*2}}+\frac{\partial^2\psi^*}{\partial z^{*2}}=K^2\sinh\psi^* \tag{5}$$

where $\psi^*=e\mathcal{Z}\psi/k_BT_{av}$, $y^*=y/H$, $z^*=z/H$, and $K=H/\lambda_D$ is the dimensionless Debye-Hückel parameter with $\lambda_D=\left(2n_0e^2\mathcal{Z}^2/\varepsilon k_BT_{av}\right)^{-1/2}$ being the Debye length, a measure of the extent of EDL. For low potentials, namely $\psi^*\leqslant 1$, $\sinh\psi^*$ in the right hand side of Eq. (5) may be approximated by ψ^*. This approximation is known as Debye–Hückel linearization. It is noted that for typical values of $\mathcal{Z}=1$ and $T_{av}=298$ K, this approximation is valid when the electrical potential is below 25.7 mV. Performing the Debye–Hückel linearization and using the boundary condition of $\psi^*_{\mathbb{P}}=\zeta^*$, with $\mathbb{P}$ denoting the duct boundary and $\zeta^*=e\mathcal{Z}\zeta/k_BT_{av}$ representing the dimensionless zeta potential, we come up with the following electrical potential distribution

$$\psi^*=\zeta^*\frac{\cosh(Ky^*)}{\cosh K}+2\zeta^*K^2\sum_{n=0}^{\infty}\frac{(-1)^n\cos(\gamma_ny^*)\cosh(\eta_nz^*)}{\gamma_n\eta_n^2\cosh(\eta_n\alpha)} \tag{6}$$

where $\gamma_n=(2n+1)\pi/2$, $\eta_n^2=K^2+\gamma_n^2$, and $\alpha=W/H$ stands for the channel aspect ratio.

2.3. Velocity distribution

The momentum exchange through the flow field is governed by the Cauchy equation

$$\rho\frac{\mathrm{D}\mathbf{u}}{\mathrm{D}t}=-\nabla p+\nabla\cdot\boldsymbol{\tau}+\mathbf{F} \tag{7}$$

in which ρ denotes the fluid density, p represents the pressure, $\boldsymbol{\tau}$ is the stress tensor, and $\mathbf{u}$ and $\mathbf{F}$ are the velocity and body force vectors, respectively. Here, the body force is given by $\rho_e\mathbf{E}$ with $\mathbf{E}=-\nabla\phi$ representing the electric field. At the fully developed conditions, the effects of the transverse velocity components are negligible compared with the axial velocity component. This, accompanied by the continuity equation, that is $\nabla\cdot\mathbf{u}=0$, results in a velocity vector of $\mathbf{u}=[u(y,z),0,0]$. Therefore, bearing in mind that $\mathrm{D}\mathbf{u}/\mathrm{D}t=0$ for a steady fully developed flow, the momentum equation in the axial direction is written as

$$\mu\left(\frac{\partial^2u}{\partial y^2}+\frac{\partial^2u}{\partial z^2}\right)=\frac{\partial p}{\partial x}-\rho_eE_x \tag{8}$$

where μ is the dynamic viscosity and $E_x=-\,\mathrm{d}\Phi/\mathrm{d}x$ is the externally applied electric field. Substituting ρ_e from Eq. (3) and performing the Debye–Hückel linearization, the dimensionless form of the momentum Eq. (8) may be written as

$$\frac{\partial^2u^*}{\partial y^{*2}}+\frac{\partial^2u^*}{\partial z^{*2}}=-2\Gamma-\frac{K^2}{\zeta^*}\psi^* \tag{9}$$

wherein $u^*=u/u_{HS}$ with $u_{HS}=-\varepsilon\zeta E_x/\mu$ being the Helmholtz–Smoluchowski electroosmotic velocity, which is the maximum possible electroosmotic velocity, and $\Gamma=u_{PD}/u_{HS}$ is the velocity scale ratio where $u_{PD}=-H^2(\partial p/\partial x)/2\mu$ stands for the pressure driven velocity scale. With zero velocity at the wall, the dimensionless velocity profile becomes

$$u^*=1+\Gamma(1-y^{*2})-\frac{\psi^*}{\zeta^*}-4\Gamma\sum_{n=0}^{\infty}\frac{(-1)^n\cos(\gamma_ny^*)\cosh(\gamma_nz^*)}{\gamma_n^3\cosh(\gamma_n\alpha)} \tag{10}$$

2.4. Temperature distribution and Nusselt number

To predict the heat transfer characteristics, we must begin with the fundamental physical law of energy conservation. The mathematical representation of this law appropriate to a fully developed electroosmotic flow is given as

$$\rho c_pu\frac{\partial T}{\partial x}=k\left(\frac{\partial^2T}{\partial x^2}+\frac{\partial^2T}{\partial y^2}+\frac{\partial^2T}{\partial z^2}\right)+s \tag{11}$$

where s denotes the rate of volumetric heat generation due to Joule heating. The Joule heating term is equal to $s=E_x^2/\sigma$ with σ being the liquid electrical resistivity given by [20]

$$\sigma=\frac{\sigma_0}{\cosh\psi^*} \tag{12}$$

in which σ_0 is the electrical resistivity of neutral liquid. The term $\cosh\psi^*$ in Eq. (12) accounts for the fact that the resistivity within EDL is lower than that of neutral liquid, due to an excess of ions close to the surface. For low zeta potentials, the ion density everywhere is not much different from that of the neutral liquid and, as a result, the electrical resistivity is very close to σ_0 everywhere. This conclusion could also be drawn from Eq. (12) as the term $\cosh\psi^*$ approaches unity for a small electrical potential. Accordingly, since we are dealing with low zeta potentials, the Joule heating term may be considered as the constant value of $s=E_x^2/\sigma_0$ [14]. The energy equation can now be modified into the following dimensionless form

$$u^*\frac{\partial\theta}{\partial x^*}=\frac{1}{Pe^2}\frac{\partial^2\theta}{\partial x^{*2}}+\frac{\partial^2\theta}{\partial y^{*2}}+\frac{\partial^2\theta}{\partial z^{*2}}+S \tag{13}$$

with the following dimensionless parameters

$$x^*=\frac{x}{HPe},\quad Pe=\frac{\rho c_pu_{HS}H}{k},\quad \theta=\frac{T-T_w}{T_0-T_w},\quad S=\frac{E_x^2H^2}{k\sigma_0(T_0-T_w)} \tag{14}$$

As noted before, the temperature field is considered in two semi-infinite regions of the channel, that is

$$\theta=\theta_1\quad\text{for } x^*\leqslant 0 \tag{15a}$$

$$\theta=\theta_2\quad\text{for } x^*\geqslant 0 \tag{15b}$$

The corresponding boundary conditions for the dimensionless energy equation are given as

$$\theta_{1,\mathbb{P}}=1 \tag{16a}$$

$$\theta_{2,\mathbb{P}}=0 \tag{16b}$$

$$\theta_1|_{x^*\to-\infty}=1+\theta_p \tag{16c}$$

$$\theta_2|_{x^*\to\infty}=\theta_p \tag{16d}$$

$$\theta_1|_{x^*=0}=\theta_2|_{x^*=0} \tag{16e}$$

$$\left.\frac{\partial\theta_1}{\partial x^*}\right|_{x^*=0}=\left.\frac{\partial\theta_2}{\partial x^*}\right|_{x^*=0} \tag{16f}$$

wherein θ_p is the solution of θ at $x^*\to\infty$ where the flow is thermally fully developed. At the fully developed conditions, the entire Joule heating is dissipated through the wall, resulting in the disappearance of the axial temperature variations. Therefore, θ_p may be obtained from the following differential equation

$$\frac{\partial^2\theta_p}{\partial y^{*2}}+\frac{\partial^2\theta_p}{\partial z^{*2}}+S=0 \tag{17a}$$

$$\theta_{p,\mathbb{P}}=0 \tag{17b}$$

It can be shown that the solution of Eq. (17a) subject to the boundary condition (17b) is as follows

$$\theta_p=\frac{S}{2}(1-y^{*2})+2S\sum_{n=0}^{\infty}\frac{(-1)^{n+1}\cos(\gamma_n y^*)\cosh(\gamma_n z^*)}{\gamma_n^3\cosh(\gamma_n\alpha)} \tag{18}$$

For constructing the general solution of Eq. (13), the boundary conditions (16c) and (16d) are the key factors. They suggest that the solutions for the upstream and downstream regions should contain the terms $1+\theta_p$ and θ_p, respectively. They also dictate that the remaining terms vanish at the regions far away from the entrance. This, accompanied by the general characteristics of the partial differential Eq. (13), reveals that the remaining terms should contain exponential functions of the axial coordinate. Finally, our experience from solving the partial differential equations remind us that the remaining terms should be in the form of infinite series of eigenfunctions. The general solution of Eq. (13) in the upstream and downstream regions is therefore written as

$$\theta_1=1+\theta_p+\sum_{n=1}^{\infty}A_n\mathbb{F}_n(y^*,z^*)e^{\lambda_n^2x^*} \tag{19a}$$

$$\theta_2=\theta_p+\sum_{n=1}^{\infty}B_n\mathbb{G}_n(y^*,z^*)e^{-\beta_n^2x^*} \tag{19b}$$

in which A_n and B_n are the constants of integration and λ_n and β_n designate the real eigenvalues associated with the eigenfunctions $\mathbb{F}_n$ and $\mathbb{G}_n$, respectively. By substituting Eqs. (19a) and (19b) into Eq. (13) with the consideration of Eq. (17a), it is straightforward to show that the functions $\mathbb{F}_n$ and $\mathbb{G}_n$ satisfy the following differential equations

$$\frac{\partial^2\mathbb{F}_n}{\partial y^{*2}}+\frac{\partial^2\mathbb{F}_n}{\partial z^{*2}}+\lambda_n^2\left[\frac{\lambda_n^2}{Pe^2}-u^*(y^*,z^*)\right]\mathbb{F}_n=0 \tag{20a}$$

$$\frac{\partial^2\mathbb{G}_n}{\partial y^{*2}}+\frac{\partial^2\mathbb{G}_n}{\partial z^{*2}}+\beta_n^2\left[\frac{\beta_n^2}{Pe^2}+u^*(y^*,z^*)\right]\mathbb{G}_n=0 \tag{20b}$$

with the following boundary conditions

$$\mathbb{F}_{n,\mathbb{P}}=0 \tag{21a}$$

$$\mathbb{G}_{n,\mathbb{P}}=0 \tag{21b}$$

which are obtainable from applying the boundary conditions (16a) and (16b) to Eqs. (19a) and (19b), respectively. The fundamental problem is then to determine the eigenvalues λ_n and β_n, the eigenfunctions $\mathbb{F}_n$ and $\mathbb{G}_n$, and the coefficients A_n and B_n. The main difficulty here is that the eigenfunctions $\mathbb{F}_n$ and $\mathbb{G}_n$ are not mutually orthogonal by referring to the standard Sturm–Liouville problem, since the eigenvalues occur nonlinearly in (20a) and (20b). However, still it is possible to seek orthogonality conditions for the problem and consequently obtain the coefficients A_n and B_n. Substituting the solutions (19a) and (19b) into Eqs. (16e) and (16f), which represent the continuity of temperature and its first derivative at the junction $x^*=0$, one may obtain the following equations

$$1+\sum_{n=1}^{\infty}A_n\mathbb{F}_n(y^*,z^*)=\sum_{n=1}^{\infty}B_n\mathbb{G}_n(y^*,z^*) \tag{22a}$$

$$\sum_{n=1}^{\infty}\lambda_n^2A_n\mathbb{F}_n(y^*,z^*)=-\sum_{n=1}^{\infty}\beta_n^2B_n\mathbb{G}_n(y^*,z^*) \tag{22b}$$

Multiplying Eq. (22a) by $(\beta_m^2/Pe^2+u^*)\mathbb{G}_m$ and integrating the resultant equation over the dimensionless channel cross section, one may obtain

$$\begin{aligned}\int_{\mathbb{A}^*}\left(\frac{\beta_m^2}{Pe^2}+u^*\right)\mathbb{G}_m d\mathbb{A}^* &= B_m\int_{\mathbb{A}^*}\left(\frac{\beta_m^2}{Pe^2}+u^*\right)\mathbb{G}_m^2 d\mathbb{A}^*\\ &-\sum_{n=1}^{\infty}A_n\int_{\mathbb{A}^*}\left(\frac{\beta_m^2}{Pe^2}+u^*\right)\mathbb{G}_m\mathbb{F}_n d\mathbb{A}^*\\ &+\sum_{\substack{n=1\\(n\neq m)}}^{\infty}B_n\int_{\mathbb{A}^*}\left(\frac{\beta_m^2}{Pe^2}+u^*\right)\mathbb{G}_m\mathbb{G}_n d\mathbb{A}^*\end{aligned} \tag{23}$$

where $\mathbb{A}^*=\mathbb{A}/H^2$ stands for the dimensionless cross sectional area. By multiplying Eq. (20b) by $\mathbb{G}_m$ and subtracting it from a similar equation for $\mathbb{G}_m$ multiplied by $\mathbb{G}_n$, and integrating the resultant equation over $\mathbb{A}^*$, the following relation is achieved

$$\begin{aligned}&(\beta_m^2-\beta_n^2)\int_{\mathbb{A}^*}\left(\frac{\beta_m^2+\beta_n^2}{Pe^2}+u^*\right)\mathbb{G}_m\mathbb{G}_n d\mathbb{A}^*\\ &=\int_{\mathbb{A}^*}[\mathbb{G}_m\nabla^*\cdot\nabla^*\mathbb{G}_n-\mathbb{G}_n\nabla^*\cdot\nabla^*\mathbb{G}_m]d\mathbb{A}^*\\ &=\int_{\mathbb{P}^*}\left(\mathbb{G}_m\frac{\partial\mathbb{G}_n}{\partial\mathbb{m}^*}-\mathbb{G}_n\frac{\partial\mathbb{G}_m}{\partial\mathbb{m}^*}\right)d\mathbb{P}^*\end{aligned} \tag{24}$$

where $\nabla^*=H\nabla$, $\mathbb{P}^*=\mathbb{P}/H$, and $\mathbb{m}^*=\mathbb{m}/H$ denotes the nondimensional form of the outward normal direction to the wall. It should be pointed out that, here and in what follows, the Del operator is assumed to operate only in yz plane. Using the boundary condition (21b), it is straightforward to obtain the following orthogonality condition from Eq. (24)

$$\int_{\mathbb{A}^*}\left(\frac{\beta_m^2+\beta_n^2}{Pe^2}+u^*\right)\mathbb{G}_m\mathbb{G}_n d\mathbb{A}^*\begin{cases}=0 & \text{if } n\neq m\\ \neq 0 & \text{if } n=m\end{cases} \tag{25}$$

The integral in the last term of second member of Eq. (23) can be rewritten using the above orthogonality condition and Eq. (23) becomes

$$\begin{aligned}\int_{\mathbb{A}^*}\left(\frac{\beta_m^2}{Pe^2}+u^*\right)\mathbb{G}_m d\mathbb{A}^* &= B_m\int_{\mathbb{A}^*}\left(\frac{\beta_m^2}{Pe^2}+u^*\right)\mathbb{G}_m^2 d\mathbb{A}^*\\ &-\sum_{n=1}^{\infty}A_n\int_{\mathbb{A}^*}\left(\frac{\beta_m^2}{Pe^2}+u^*\right)\mathbb{G}_m\mathbb{F}_n d\mathbb{A}^*\\ &-\sum_{\substack{n=1\\(n\neq m)}}^{\infty}B_n\frac{\beta_n^2}{Pe^2}\int_{\mathbb{A}^*}\mathbb{G}_m\mathbb{G}_n d\mathbb{A}^*\end{aligned} \tag{26}$$

Furthermore, by multiplying Eq. (22b) by $\mathbb{G}_m/Pe^2$ and integrating over $\mathbb{A}^*$, we obtain

$$-\sum_{n=1}^{\infty}B_n\frac{\beta_n^2}{Pe^2}\int_{\mathbb{A}^*}\mathbb{G}_m\mathbb{G}_n d\mathbb{A}^*=\sum_{n=1}^{\infty}A_n\frac{\lambda_n^2}{Pe^2}\int_{\mathbb{A}^*}\mathbb{G}_m\mathbb{F}_n d\mathbb{A}^* \tag{27}$$

After some manipulation, Eq. (26) takes the following form, by utilizing Eq. (27)

$$\int_{\mathbb{A}^*}\left(\frac{\beta_m^2}{Pe^2}+u^*\right)\mathbb{G}_m d\mathbb{A}^*=B_m\int_{\mathbb{A}^*}\left(\frac{2\beta_m^2}{Pe^2}+u^*\right)\mathbb{G}_m^2 d\mathbb{A}^*+\sum_{n=1}^{\infty}A_nF_{n,m} \tag{28}$$

where

$$F_{n,m}=\int_{\mathbb{A}^*}\left(\frac{\lambda_n^2-\beta_m^2}{Pe^2}-u^*\right)\mathbb{G}_m\mathbb{F}_n d\mathbb{A}^* \tag{29}$$

The previous technique can again be used, by multiplying Eq. (22a) this time by $(\lambda_m^2/Pe^2-u^*)\mathbb{F}_m$ and also utilizing similar property as given by Eq. (25) for $\mathbb{F}_n$, resulting in the following equation

$$\int_{\mathbb{A}^*}\left(\frac{\lambda_m^2}{Pe^2}-u^*\right)\mathbb{F}_m\mathrm{d}\mathbb{A}^*=-A_m\int_{\mathbb{A}^*}\left(\frac{2\lambda_m^2}{Pe^2}-u^*\right)\mathbb{F}_m^2\mathrm{d}\mathbb{A}^*+\sum_{n=1}^{\infty}B_nF_{m,n} \tag{30}$$

It is easy to show that $F_{n,m}$ and $F_{m,n}$ are zero for any m and n. Just one should consider two solutions $\mathbb{F}_n$ and $\mathbb{G}_m$ of Eqs. (20a) and (20b), multiplying the first one by $\mathbb{G}_m$ and the second one by $\mathbb{F}_n$ and then subtracting and integrating over $\mathbb{A}^*$ to obtain

$$\begin{aligned}&\int_{\mathbb{A}^*}[\mathbb{G}_m\nabla^*\cdot\nabla^*\mathbb{F}_n-\mathbb{F}_n\nabla^*\cdot\nabla^*\mathbb{G}_m]\mathrm{d}\mathbb{A}^*\\&+(\lambda_n^2+\beta_m^2)\int_{\mathbb{A}^*}\\&\times\left(\frac{\lambda_n^2-\beta_m^2}{Pe^2}-u^*\right)\mathbb{G}_m\mathbb{F}_n\mathrm{d}\mathbb{A}^*\\&=\int_{\mathbb{P}^*}\left(\mathbb{G}_m\frac{\partial\mathbb{F}_n}{\partial\mathbb{m}^*}-\mathbb{F}_n\frac{\partial\mathbb{G}_m}{\partial\mathbb{m}^*}\right)\mathrm{d}\mathbb{P}^*+(\lambda_n^2+\beta_m^2)F_{n,m}=0\end{aligned} \tag{31}$$

Using the boundary conditions given by Eq. (21), it is trivial to verify that $F_{n,m}$, and in a similar way, $F_{m,n}$ are zero for any m and n. Finally, from Eqs. (28) and (30) one may get the expressions for A_n and B_n as ratios of two integrals, i.e.,

$$A_n=-\frac{\int_{\mathbb{A}^*}\left(\frac{\lambda_n^2}{Pe^2}-u^*\right)\mathbb{F}_n\mathrm{d}\mathbb{A}^*}{\int_{\mathbb{A}^*}\left(\frac{2\lambda_n^2}{Pe^2}-u^*\right)\mathbb{F}_n^2\mathrm{d}\mathbb{A}^*} \tag{32a}$$

$$B_n=\frac{\int_{\mathbb{A}^*}\left(\frac{\beta_n^2}{Pe^2}+u^*\right)\mathbb{G}_n\mathrm{d}\mathbb{A}^*}{\int_{\mathbb{A}^*}\left(\frac{2\beta_n^2}{Pe^2}+u^*\right)\mathbb{G}_n^2\mathrm{d}\mathbb{A}^*} \tag{32b}$$

To calculate the Nusselt number, first the dimensionless bulk temperature should be evaluated by the following integration

$$\theta_{b,i}=\frac{\int_{\mathbb{A}^*}u^*\theta_i\mathrm{d}\mathbb{A}^*}{\int_{\mathbb{A}^*}u^*\mathrm{d}\mathbb{A}^*} \tag{33}$$

Based on the definition, the Nusselt number is written as

$$\begin{aligned}Nu_i&=\frac{h_iD_h}{k}=\frac{4HW}{H+W}\frac{\left(\frac{\partial T_i}{\partial\mathbb{m}}\right)_{\mathbb{P},av}}{T_{\mathbb{P},i}-T_{b,i}}\\&=\frac{4\alpha}{(1+\alpha)^2}\frac{\int_0^1\frac{\partial\theta_i}{\partial z^*}(y^*,\alpha)\mathrm{d}y^*+\int_0^\alpha\frac{\partial\theta_i}{\partial y^*}(1,z^*)\mathrm{d}z^*}{\theta_{\mathbb{P},i}-\theta_{b,i}}\end{aligned} \tag{34}$$

Our formulation is now complete except for the eigenvalues λ_n and β_n and the eigenfunctions $\mathbb{F}_n$ and $\mathbb{G}_n$ to be determined. Since we are interested in the downstream region, only determination of β_n and $\mathbb{G}_n$, which is the subject of the next section, suffices.

2.5. Solution of the eigenvalue problem

2.5.1. General solution

The variational calculus procedure is chosen for treating the eigenvalue problem (20b). According to this method, the solution $\mathbb{G}_n$ of Eq. (20b) also minimizes the following integral [28]

$$I=\int_{\mathbb{A}^*}\left[\left(\frac{\partial\mathbb{G}_n}{\partial y^*}\right)^2+\left(\frac{\partial\mathbb{G}_n}{\partial z^*}\right)^2-\beta_n^2\left(\frac{\beta_n^2}{Pe^2}+u^*\right)\mathbb{G}_n^2-\frac{1}{2}\left(\frac{\partial^2\mathbb{G}_n^2}{\partial y^{*2}}+\frac{\partial^2\mathbb{G}_n^2}{\partial z^{*2}}\right)\right]\mathrm{d}\mathbb{A}^* \tag{35}$$

Next, $\mathbb{G}_n$ is considered to be composed of a complete and linearly independent set of basis functions $f_j(y^*,z^*)$ as

$$\mathbb{G}_n=\sum_{j=1}^{N}d_{nj}f_j \tag{36}$$

It is worth noting that the choice of the basis functions is arbitrary provided the boundary condition (21b) is satisfied. Here, the following functionality is assumed for f_j

$$f_j(y^*,z^*)=\cos[(2l_j+1)\pi y^*/2]\cos[(2m_j+1)\pi z^*/2\alpha] \tag{37}$$

where $l_j=0,1,2,\cdots$, $m_j=0,1,2,\cdots$, and $N=(l_{j,max}+1)(m_{j,max}+1)$. Following the substitution of $\mathbb{G}_n$ from Eq. (36) into Eq. (35), the minimization of $I(d_{n1}, d_{n2},\cdots,d_{nN})$ requires having

$$\frac{\partial I}{\partial d_{ni}}=0\quad\text{for } i=1,2,\cdots,N \tag{38}$$

This differentiation results in the following relation

$$\begin{aligned}&2\int_{\mathbb{A}^*}\left[\frac{\partial\mathbb{G}_n}{\partial y^*}\frac{\partial f_i}{\partial y^*}+\frac{\partial\mathbb{G}_n}{\partial z^*}\frac{\partial f_i}{\partial z^*}-\beta_n^2\left(\frac{\beta_n^2}{Pe^2}+u^*\right)\mathbb{G}_nf_i\right]\mathrm{d}\mathbb{A}^*\\&-\int_{\mathbb{A}^*}\left[\frac{\partial^2(\mathbb{G}_nf_i)}{\partial y^{*2}}+\frac{\partial^2(\mathbb{G}_nf_i)}{\partial z^{*2}}\right]\mathrm{d}\mathbb{A}^*=0\quad\text{for } i=1,2,\cdots,N\end{aligned} \tag{39}$$

which can be rewritten as

$$\begin{aligned}&2\int_{\mathbb{A}^*}\left[\frac{\partial^2\mathbb{G}_n}{\partial y^{*2}}+\frac{\partial^2\mathbb{G}_n}{\partial z^{*2}}+\beta_n^2\left(\frac{\beta_n^2}{Pe^2}+u^*\right)\mathbb{G}_n\right]f_i\mathrm{d}\mathbb{A}^*\\&-2\int_{\mathbb{A}^*}\nabla^*\cdot(f_i\nabla^*\mathbb{G}_n)\mathrm{d}\mathbb{A}^*\\&+\int_{\mathbb{A}^*}\nabla^{*2}(\mathbb{G}_nf_i)\mathrm{d}\mathbb{A}^*=0\quad\text{for } i=1,2,\cdots,N\end{aligned} \tag{40}$$

The last two terms in Eq. (40) can be written as

$$\begin{aligned}&-2\int_{\mathbb{A}^*}\nabla^*\cdot(f_i\nabla^*\mathbb{G}_n)\mathrm{d}\mathbb{A}^*+\int_{\mathbb{A}^*}\nabla^{*2}(\mathbb{G}_nf_i)\mathrm{d}\mathbb{A}^*\\&=-\int_{\mathbb{A}^*}[\nabla^*\cdot(f_i\nabla^*\mathbb{G}_n)-\nabla^*\cdot(\mathbb{G}_n\nabla^*f_i)]\mathrm{d}\mathbb{A}^*\\&=-\int_{\mathbb{P}^*}\left(f_i\frac{\partial\mathbb{G}_n}{\partial\mathbb{m}^*}-\mathbb{G}_n\frac{\partial f_i}{\partial\mathbb{m}^*}\right)\mathrm{d}\mathbb{P}^*\end{aligned} \tag{41}$$

Since both f_i and $\mathbb{G}_n$ should satisfy the boundary condition (21b), the right-hand side of Eq. (41), and as a result, the two last terms in Eq. (40) vanish. Then, after substitution of $\mathbb{G}_n$ from Eq. (36) into Eq. (40), it reduces to

$$\begin{aligned}&\sum_{j=1}^{N}d_{nj}\left[\int_{\mathbb{A}^*}\left(\frac{\partial^2f_j}{\partial y^{*2}}+\frac{\partial^2f_j}{\partial z^{*2}}\right)f_i\mathrm{d}\mathbb{A}^*+\beta_n^2\int_{\mathbb{A}^*}u^*f_jf_i\mathrm{d}\mathbb{A}^*+\frac{\beta_n^4}{Pe^2}\int_{\mathbb{A}^*}f_jf_i\mathrm{d}\mathbb{A}^*\right]\\&=0\quad\text{for } i=1,2,\cdots,N\end{aligned} \tag{42}$$

Eq. (42) represents a system of N equations of $N+1$ unknowns including $d_{n1},d_{n2},\cdots,d_{nN}$, and β_n. This equation may be written in matrix form as

$$(\mathbf{A}+\beta^2\mathbf{B}+\beta^4\mathbf{C})\mathbf{d}=0 \tag{43}$$

wherein the symmetric matrices **A**, **B**, and **C** have the elements

$$a_{ij}=\int_{\mathbb{A}^*}\left(\frac{\partial^2f_j}{\partial y^{*2}}+\frac{\partial^2f_j}{\partial z^{*2}}\right)f_i\mathrm{d}\mathbb{A}^* \tag{44a}$$

$$b_{ij}=\int_{\mathbb{A}^*}u^*f_jf_i\mathrm{d}\mathbb{A}^* \tag{44b}$$

and

$$c_{ij}=\int_{\mathbb{A}^*}\frac{f_jf_i}{Pe^2}\mathrm{d}\mathbb{A}^* \tag{44c}$$

The vector **d** in Eq. (43) stands for the coefficients $d_1, d_2,\cdots,d_N$. Since Eq. (43) is not a classical eigenvalue problem, it requires a modified mathematical procedure to be solved. As noted by Haji-Sheikh [28], this equation can be reduced to a classical eigenvalue problem by introducing new vectors **v** and **w** so that $\mathbf{w}=\beta^2\mathbf{d}=\beta^2\mathbf{v}$. We will therefore have the following eigenvalue problem

$$\begin{bmatrix}\mathbf{0}&\mathbf{I}\\\mathbf{A}&\mathbf{B}\end{bmatrix}\begin{bmatrix}\mathbf{v}\\\mathbf{w}\end{bmatrix}-\beta^2\begin{bmatrix}\mathbf{I}&0\\0&-\mathbf{C}\end{bmatrix}\begin{bmatrix}\mathbf{v}\\\mathbf{w}\end{bmatrix}=0 \tag{45}$$

where **I** is the identity matrix. Eq. (45) can be solved for the eigenvalues β_n^2 and eigenvectors $\mathbf{d}_n$ using standard computational methods. It is noteworthy that since the sizes of the matrices in Eq. (45) are two times of the original ones, the solution of Eq. (45) provides $2N$ number of the eigenvalues β_n^2, N of them being positive and the others being negative. Based on the physics of the problem, only the positive ones can be used in calculations of the temperature field for $x \geqslant 0$.

2.5.2. Analytical solution for electroosmotic flow under thin EDL limit

When the Debye length is much smaller than the channel length scale the electroosmotic velocity profile is nearly uniform with a large velocity gradient near the wall. Accordingly, for a high value of K, the velocity profile for the present problem can efficiently be represented by $u^* = 1$, provided no pressure gradient is applied. By this simple velocity profile, an analytical treatment of Eq. (20b) will be possible. It is straightforward to show that the eigenfunction $\mathbb{G}_n$ and eigenvalue β_n under a uniform velocity profile assumption are given as

$$\mathbb{G}_n = \cos[(2l_n+1)\pi y^*/2]\cos[(2m_n+1)\pi z^*/2\alpha] \tag{46}$$

$$\beta_n^2 = \frac{Pe\sqrt{Pe^2+(2l_n+1)^2\pi^2+(2m_n+1)^2\pi^2/\alpha^2}-Pe^2}{2} \tag{47}$$

where $l_n = 0,1,2,\cdots$ and $m_n = 0,1,2,\cdots$. The following expression is also obtained for B_n by inserting Eqs. (46) and (47) into Eq. (32b)

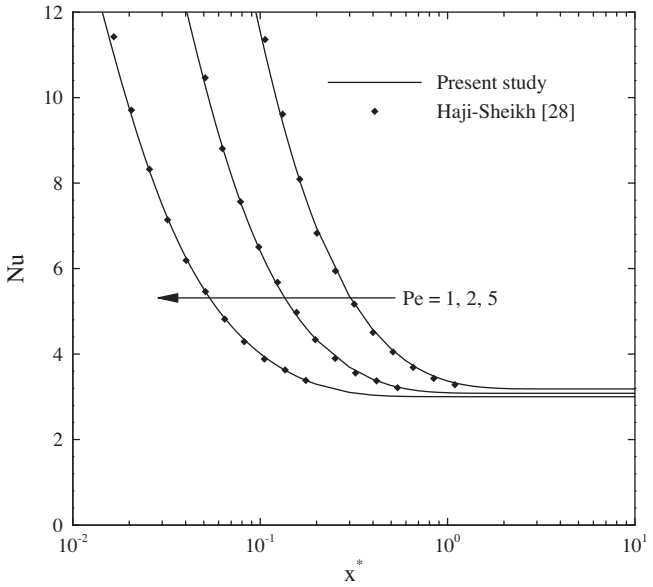

Fig. 2. Comparison between the present Nusselt numbers for the special case of the pressure driven flow with no internal heating in a square duct against those reported by Haji-Sheikh [28].

$$B_n = 8(-1)^{l_n+m_n}\frac{(2m_n+1)/(2l_n+1)\alpha^2+(2l_n+1)/(2m_n+1)}{Pe^2+(2l_n+1)^2\pi^2+(2m_n+1)^2\pi^2/\alpha^2-Pe\sqrt{Pe^2+(2l_n+1)^2\pi^2+(2m_n+1)^2\pi^2/\alpha^2}} \tag{48}$$

3. Method validation

Before proceeding with the discussion of results, a comparison against existing literature data is needed for validation of the method developed. One of the best choices for comparison are the data reported by Haji-Sheikh [28] for thermally developing Poiseuille flow in a rectangular duct. Since these data have been obtained by assuming no internal heat generation, we should set $S = 0$. In addition, the velocity scale ratio should tend infinity for the electroosmotic part of velocity to vanish. Moreover, the velocity profile is normalized by the mean velocity because Haji-Sheikh [28] has used the mean velocity for non-dimensionalization. For a better comparison, since he used 120 eigenvalues in the computations, both $l_{j,max}$ and $m_{j,max}$ are set to 10 to provide 121 eigenvalues. Fig. 2 shows both the present Nusselt number values and those reported by Haji-Sheikh [28] at different Peclet numbers and reveals a good agreement between them.

Since the above comparison was for no internal heating case, one cannot be sure that the results are free of error until a complete check in the presence of the Joule heating is made. Table 1 compares the fully developed Nusselt number values for purely electroosmotic flow in a channel with a large aspect ratio, that is $\alpha \to \infty$, against those predicted using the expression given by Sadeghi and Saidi [17] for a parallel plate channel. As observed, the relative error for all the cases being considered is only about 0.2% which is quite acceptable especially because the present results are obtained by means of the numerical integration. Furthermore, although we consider a quite large aspect ratio for the channel to imitate a slit but there still will be corner effects included in the calculations. It should be pointed out that the comparison is only made for $S = -1$ because the research work done by Sadeghi and Saidi [17] is generally dealing with a constant heat flux boundary condition and it only reduces to a constant temperature boundary condition when $S = -1$.

Besides the validation of results, since the convergence of the series solution becomes more difficult by decreasing the axial position, a convergence analysis is needed to find out the region in which the results are accurate. Fig. 3 illustrates the local Nusselt number values of the purely electroosmotic flow in a square duct obtained by using different numbers of eigenvalues. The data is provided for $Pe = 1$, the minimum Peclet number which will be used in presenting the results, for which the error is maximum. As observed in the figure, the discrepancy between the results obtained by setting $l_{j,max} = m_{j,max} = 50$ and those of $l_{j,max} = m_{j,max} = 60$ is not significant for $x^* \geqslant 0.02$. The maximum discrepancy in this

Table 1
Comparison between the present fully developed Nusselt number values against literature data for the special case of purely electroosmotic flow with $\alpha \to \infty$ and $S = -1$.

K	Nu		Error (%)
	Present study	Ref. [17]	
5	10.5961	10.6197	0.2222
10	11.0750	11.0997	0.2225
20	11.4563	11.4818	0.2221
40	11.6954	11.7214	0.2218
80	11.8291	11.8555	0.2227

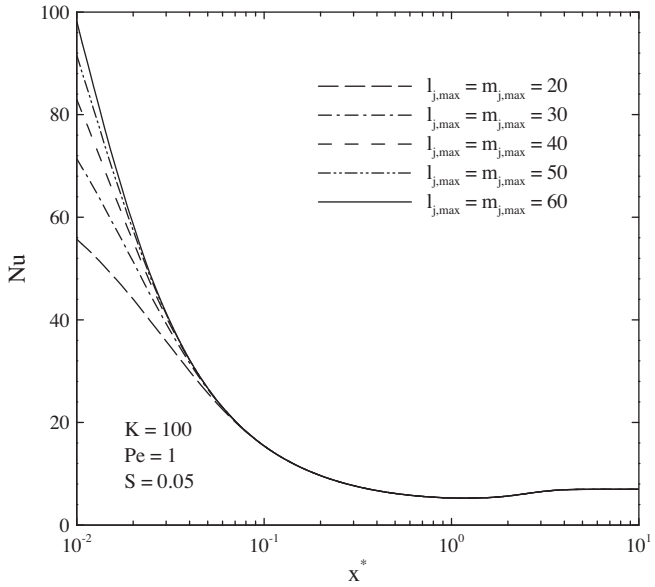

Fig. 3. Local Nusselt number values of the purely electroosmotic flow in a square duct obtained by using different numbers of eigenvalues.

range, occurred for $x^* = 0.02$, is only about 2% which is quite reasonable for Graetz type problems, especially because only the graphical data is presented here. Therefore, we set $l_{j,max} = m_{j,max} = 50$ and limit the presentation of the Nusselt number values to this range of the axial position. For the bulk temperature, this region is extended to $x^* \geqslant 0.01$ because it is calculated with much more accuracy.

4. Results and discussion

A numerical code developed in MATLAB was used to perform the numerical calculations. All the numerical integrations were carried out by means of the Cavalieri–Simpson method for integration. This method gives a good estimate for the value of an integral with relatively little computation. The eigenvalues and eigenfunctions were obtained for $Pe = 1,2,4$, the dimensionless Debye–Hückel parameters of $K = 4,20,100$, the channel aspect ratios of $\alpha = 1,2,3,4,5$, and $\Gamma = -1,0,1$.

The presentation of results begins with giving the 3D plots of the dimensionless temperature for purely electroosmotic flow through a square duct in Fig. 4. The graphs are presented at different axial positions while keeping $K = 20$, $Pe = 4$, and $S = -0.01$. The negative value of S implies that electroosmosis has been used for heat removal purpose, that is $T_0 < T_w$. Different temperature patterns are observed in the figure for different axial positions. Near

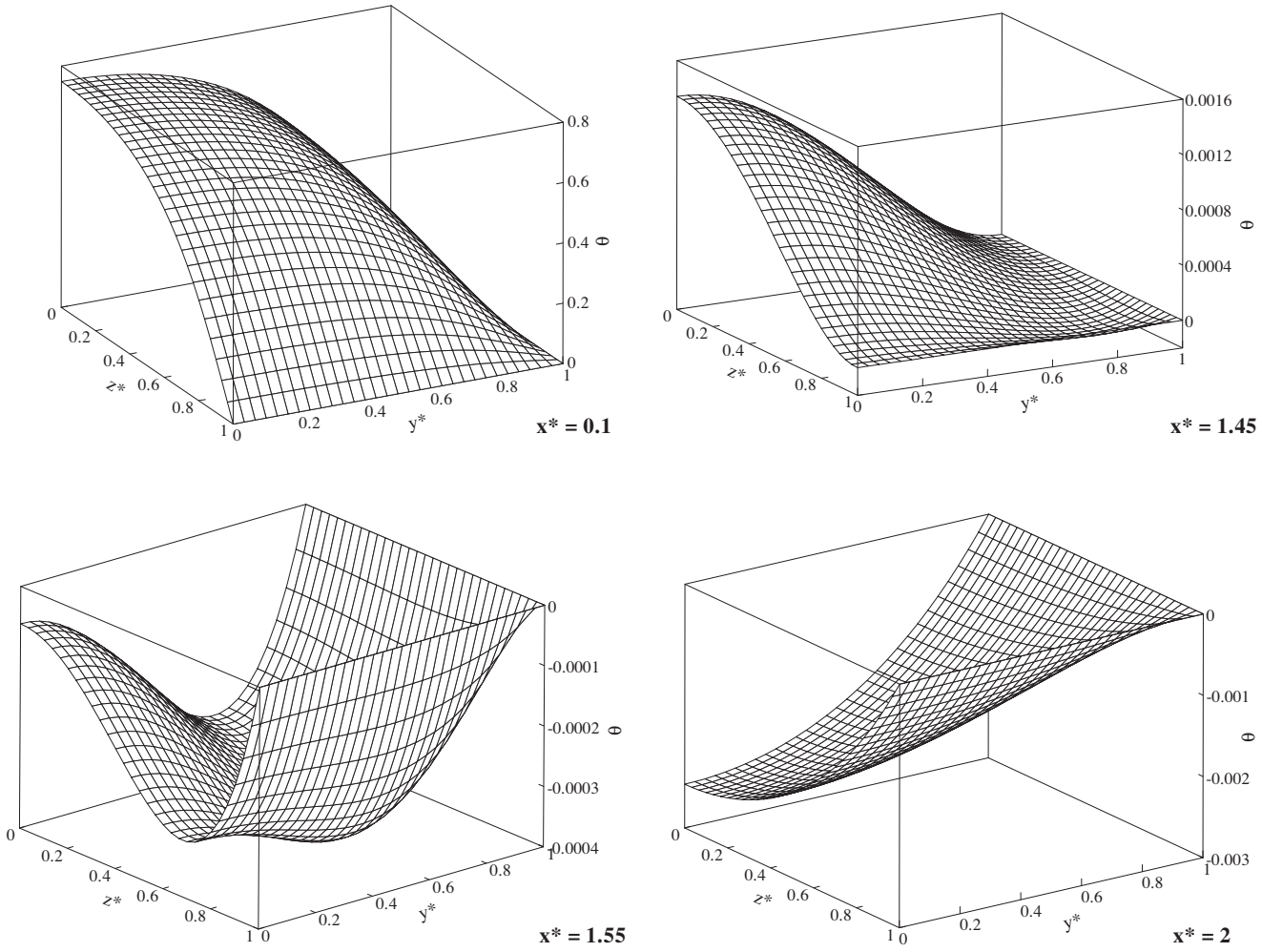

Fig. 4. Dimensionless temperature distribution at different axial positions for purely electroosmotic flow in a square duct at $K = 20$, $Pe = 4$, and $S = -0.01$.

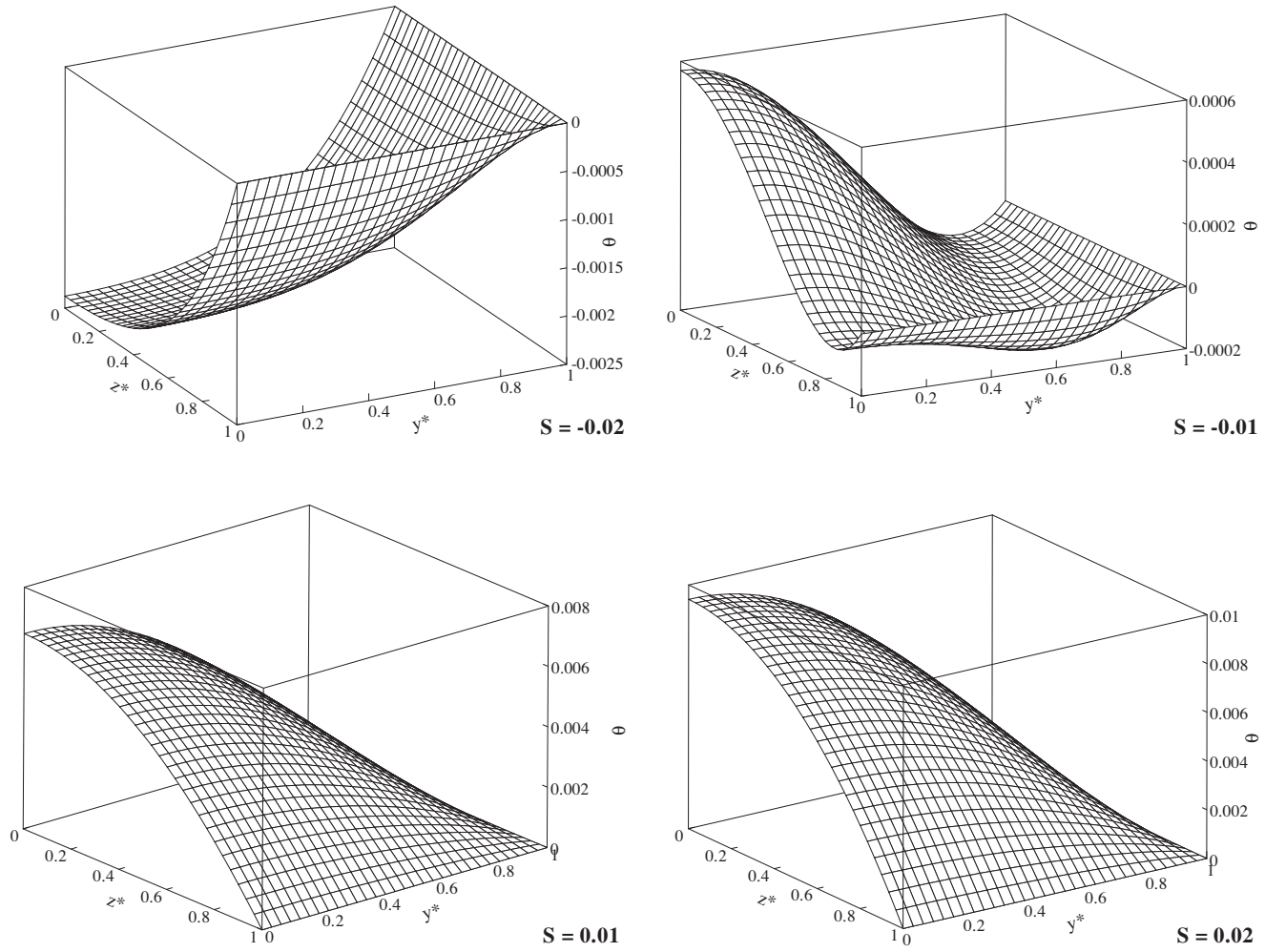

Fig. 5. Dimensionless temperature distribution at different values of S for purely electroosmotic flow in a square duct at $K = 20$, $Pe = 4$, and $x^* = 1.5$.

the entrance, that is at $x^* = 0.1$, the temperature profile is of a nearly parabolic shape. As expected, the temperature is lower than T_w everywhere reflecting in a positive θ. This is therefore a region in which an efficient cooling is possible. As the fluid moves downstream its temperature is increased because of cooling the wall and, as a result, the wall heat flux decreases gradually. This reduction is continued until $x^* \cong 1.45$ at which the average wall heat flux vanishes. This point, corresponding to $x \cong 6H$, is the end of the cooled section of the duct and the rest of channel is left uncooled. Although for higher axial positions the wall heat flux is negative, i.e., heat is transferred from the fluid to the wall, the fluid temperature is increased due to the Joule heating. It should be pointed out that the negative wall heat flux in this region is not significant and it therefore will not cause a problem in cooling purposes. In fact, by assuming a temperature difference of $20K$ between the inlet fluid and the wall, the maximum temperature difference between the wall and the fluid at the fully developed conditions will be only about $0.06K$. Hence, the associated wall heat flux will be negligible and the duct and the fluid may be assumed to be in the thermal equilibrium.

Fig. 5 depicts the dimensionless temperature distribution at different values of S for purely electroosmotic flow in a square duct at $K = 20$, $Pe = 4$, and $x^* = 1.5$. As seen, while the case of $S = -0.01$ is just at the end of the cooled section of the duct, the case of $S = -0.02$ has by far passed this section. This reveals that it is possible to increase the cooled section of the duct by decreasing the Joule heating rate. In an expected behavior, a higher Joule heating effect is accompanied by higher dimensionless temperatures for the surface heating cases, that is for positive values of S.

The variations of the dimensionless bulk temperature in the axial direction at different values of Peclet number is presented in Fig. 6. The axial coordinate has been multiplied by Pe in order to remove its Peclet number dependency. As observed, the bulk temperature is a decreasing function of the axial coordinate. In the developing region, a smaller Peclet number corresponds to a lower dimensionless temperature at a given axial position. This is due to the fact that, a decrease in Peclet number, which may be thought of as a decrease in velocity, gives the fluid particles the opportunity to sense the wall effects more by means of the thermal energy diffusion. This higher effect of energy diffusion, therefore, causes a thicker thermal boundary layer and consequently a smaller entry length for a lower Peclet number, as observed in the figure. All the graphs merge together in the fully developed region, emphasizing the fact that the fully developed temperature distribution in the presence of internal heating is independent of Peclet number.

Fig. 7 illustrates the variations of the dimensionless bulk temperature in the axial direction for purely electroosmotic flow at different values of the dimensionless Debye–Hückel parameter. The predictions of the approximate method are also shown by symbols. By increasing K, EDL will be limited to smaller regions adjacent to the wall, resulting in higher velocities near the wall. Accordingly, the weight of the fluid particles near the wall, having smaller non-dimensional temperatures, in calculating θ_b is increased, resulting in smaller values of the dimensionless bulk temperature

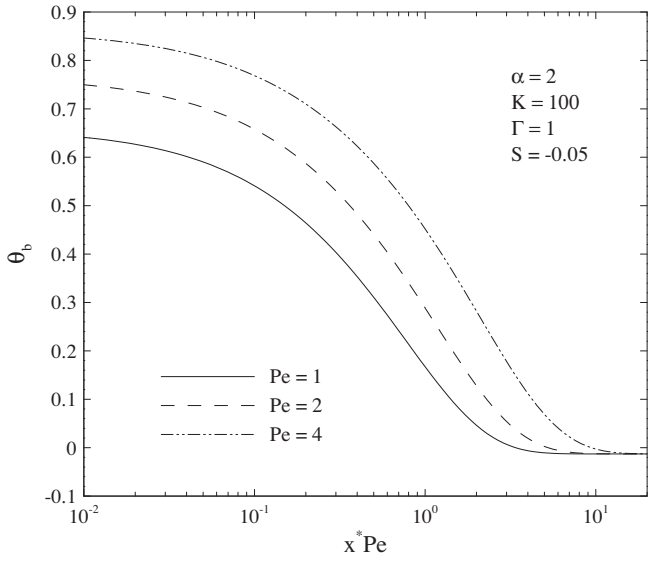

Fig. 6. Variations of the dimensionless bulk temperature in the axial direction at different values of *Pe*.

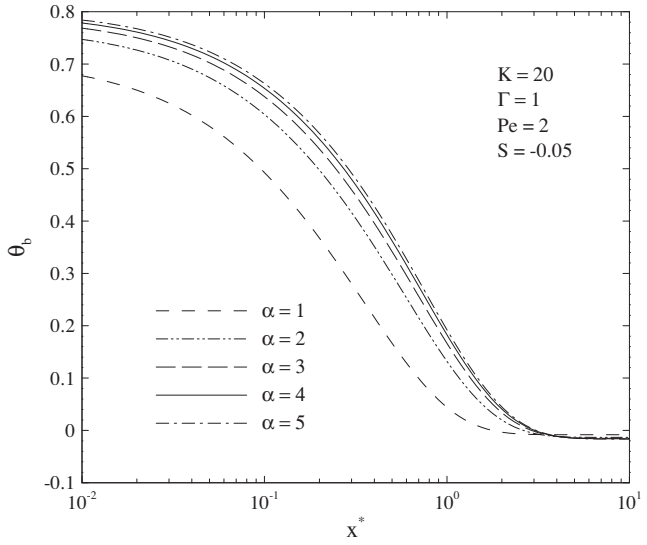

Fig. 8. Variations of the dimensionless bulk temperature in the axial direction at different channel aspect ratios.

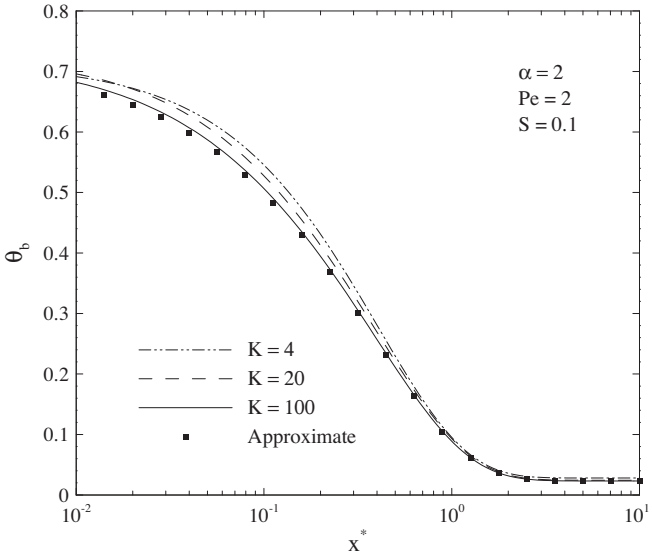

Fig. 7. Variations of the dimensionless bulk temperature in the axial direction for purely electroosmotic flow at different values of *K*.

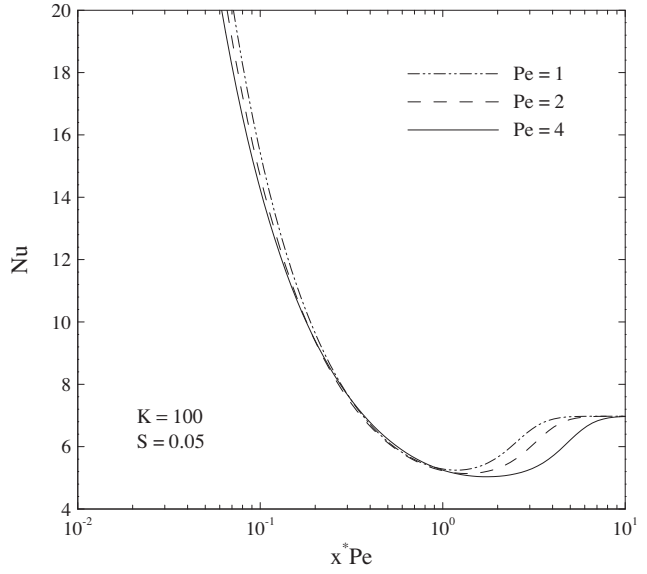

Fig. 9. Variations of Nusselt number in the axial direction for purely electroosmotic flow in a square duct at different values of the Peclet number.

for a higher *K*, as seen in the figure. It is also observed that the results obtained by assuming a uniform velocity profile are the good approximation of the exact ones for $K = 100$ especially at higher values of the axial coordinate. This means that the approximate method can be used to predict the thermal features for $K > 100$ without significant error.

The plots of θ_b versus x^* at different values of the channel aspect ratio, shown in Fig. 8, reveal that θ_b is higher for a higher α in the developing region. A channel of square cross section provides the highest energy diffusion and any deviation from a square shape gives rise to a decrease in the thermal energy diffusion. Accordingly, a higher α is accompanied by higher temperature differences between the fluid particles and the wall in the developing region. Although the same trend is observed for the fully developed region (except T_w is now smaller than T_b), another mechanism is dominant here. It is evident that an increase in α leads to a higher amount of the volume to surface ratio. Since the total Joule heating is proportional to the fluid volume and is entirely dissipated through the wall in the fully developed region, the ultimate influence of increasing α will be to increase the average wall heat flux and accordingly to increase the temperature gradients. These higher temperature gradients will therefore give rise to higher temperature differences between the wall and the bulk fluid for higher values of the channel aspect ratio.

The variations of Nusselt number in the axial direction for purely electroosmotic flow in a square duct at different values of Peclet number is given in Fig. 9. As observed, the Nusselt number decreases to a minimum before reaching the fully developed conditions and then increases to the final value. Generally speaking, an

increase in Peclet number is accompanied by a decrease in Nusselt number in the developing region. The wall heat flux is an increasing function of the Peclet number; therefore, this trend of Nusselt number is due to higher temperature differences between the wall and liquid particles for higher Peclet numbers. The functionality of the wall heat flux with Peclet number may be considered as a paradox at first glance, as the wall heat flux at each axial position is higher, whereas still higher temperature differences between the wall and fluid particles exist for higher Peclet numbers. However, attention should be given to the fact that a higher Peclet number may be thought of as a higher mass flow rate and consequently a higher energy storage capacity.

The variations of *Nu* in the axial direction at different values of *K*, given in Fig. 10, show that the Nusselt number is higher for a higher value of the dimensionless Debye–Hückel parameter. As noted previously, the dimensionless bulk temperature is a decreasing function of *K*. Furthermore, a higher *K* is accompanied by a higher wall heat flux because of higher velocities near the wall. This higher wall heat flux along with a smaller θ_b for a higher value of the dimensionless Debye–Hückel parameter are the causes of increasing *Nu* with *K*. Fig. 10 also leads one to the following conclusion: similar to the dimensionless bulk temperature, the Nusselt numbers obtained by means of the approximate method are sufficiently accurate for $K > 100$.

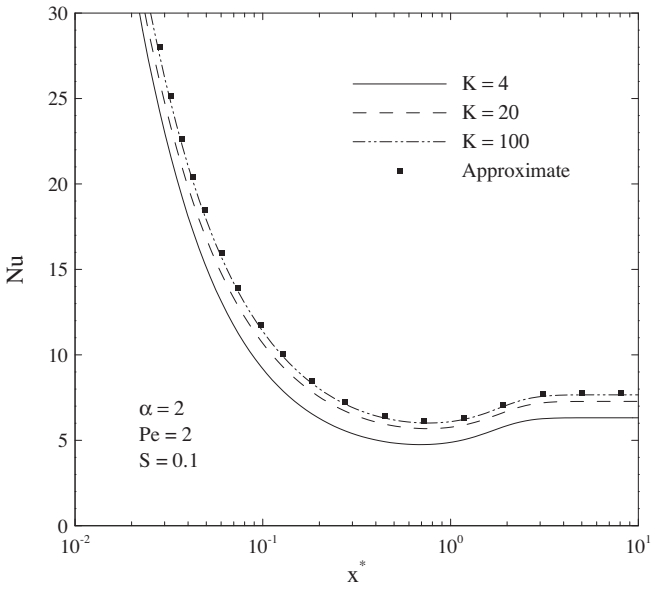

Fig. 10. Variations of Nusselt number in the axial direction for purely electroosmotic flow at different values of *K*.

Fig. 11 depicts the Nusselt number values versus the dimensionless axial coordinate at different values of the channel aspect ratio. Unlike the previous cases which were dealing with either of a purely electroosmotic flow or a pressure assisted flow, that is the case for which $\Gamma > 0$, this figure presents the results for a pressure opposed flow. From Fig. 8, one may expect a decreasing trend of *Nu* with increasing α. However, it can be seen in Fig. 11 that the opposite is true, that is an increase in α gives rise to a higher *Nu*. This is mainly because of increasing D_h, the length scale used in calculation of *Nu*, with increasing α. Furthermore, as noted before, the ratio of the total Joule heating to the channel surface is higher for a higher value of the channel aspect ratio resulting in higher amounts of the wall heat flux and, accordingly, higher Nusselt number values.

So far, we have limited the presentation of the Nusselt numbers to positive values of *S*. Fig. 12 illustrates the local Nusselt number values of a square duct at different velocity scale ratios for a negative *S*. It is observed that singularities occur in Nusselt number values. For a better explanation of this phenomenon, we make use of Fig. 4. When entering the channel, the fluid starts to be heated from the wall. The wall heat flux is thus from the wall to the fluid and the Nusselt number is positive. As the fluid is being heated, the average wall heat flux decreases gradually and reaches zero at some axial position ($x^* \cong 1.45$ for the case shown in Fig. 4), providing a zero Nusselt number. From this point forward, the direction of the wall heat flux changes due to the internal heating. However, still the bulk temperature is below the wall temperature, and, as a result, the Nusselt number is negative. In spite of the fact that the fluid is being cooled from the wall, the bulk temperature increases due to the internal heating, resulting in a higher Nusselt number with negative sign. In the limit $T_b \to T_w$, the Nusselt number with negative sign goes to infinity. At the point that the wall

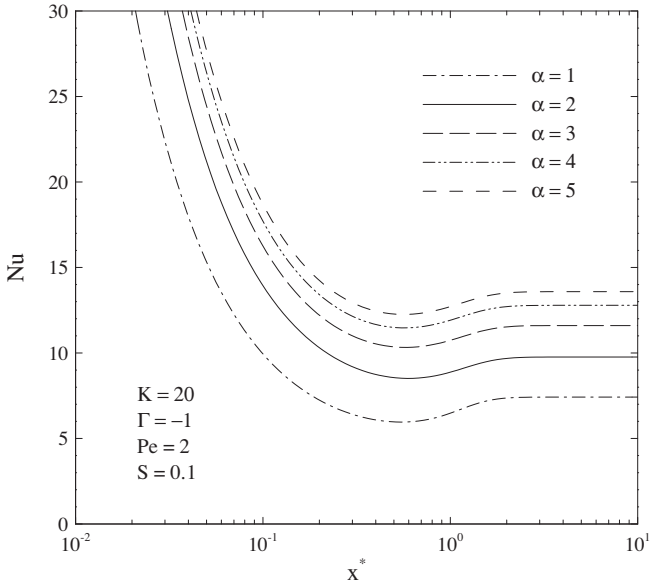

Fig. 11. Variations of Nusselt number in the axial direction at different values of α.

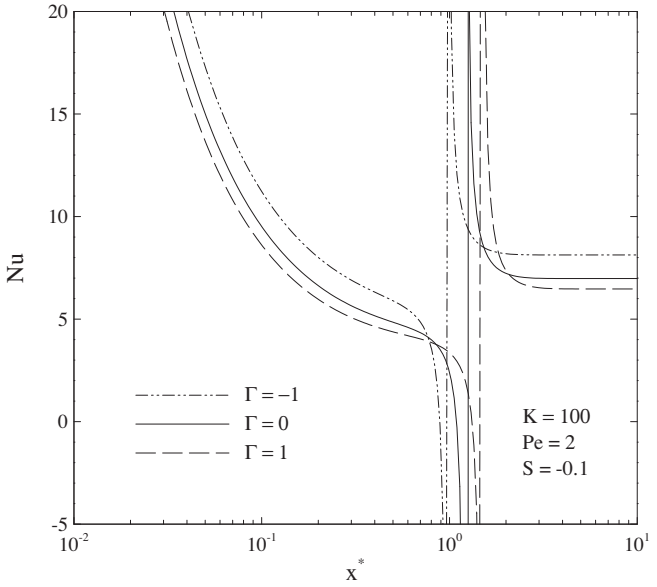

Fig. 12. Nusselt number values of a square duct versus x^* at different values of Γ.

and bulk temperatures become the same, the heat transfer rate cannot be expressed in terms of Nusselt number and a singularity occurs in Nusselt number values. More increase in the bulk temperature results in a large value of the Nusselt number with positive sign. Before reaching the fully developed conditions, the Nusselt number is decreased by increasing x^* because of increasing the difference between the bulk and wall temperatures.

5. Conclusions

Thermally developing combined electroosmotic and pressure driven flow in a rectangular microchannel was studied in this work. Because of both the Joule heating and axial conduction effects being present in electroosmotic flows, assuming a uniform inlet temperature profile is not consistent with actual heat transfer physics of the problem. Accordingly, a step change in wall temperature was considered to represent physically conceivable thermal entrance conditions. Expressions for the dimensionless distributions of the electrical potential, velocity, and temperature in the form of infinite series were presented. For general treatment of the associated eigenvalue problem, a method based on the variational calculus was used. An analytical solution was also presented for purely electroosmotic flow at thin EDL limit for which the velocity distribution can be efficiently described by a uniform profile. After validation of the results, a complete parametric study was executed. It was revealed that for the cases in which the fluid is being cooled from the wall, the Nusselt number decreases to a minimum before reaching the fully developed conditions and then increases to the final value. When the fluid is being heated from the wall, a singularity is observed in the Nusselt number values. The mechanism of this singularity point was explained in detail using energy balance. The approximate solution was also found to be accurate for predicting both the bulk mean temperature and Nusselt number as long as the dimensionless Debye–Hückel parameter is above 100. Furthermore, a higher channel aspect ratio guarantees a higher temperature difference between the wall and the bulk flow along with a higher Nusselt number. In addition, it was found that the wall heat flux is an increasing function of the Peclet number. These findings can be of immense consequence in thermal design of lab-on-a-chip based microsystems involving electroosmotic flow actuation mechanisms.

References

[1] X. Wang, S. Wang, B. Gendhar, C. Cheng, C.K. Byun, G. Li, M. Zhao, S. Liu, Electroosmotic pumps for microflow analysis, Trends Anal. Chem. 28 (1) (2009) 64–74.

[2] R.F. Probstein, Physicochemical Hydrodynamics, second ed., Wiley, New York, 1994.

[3] J.H. Masliyah, S. Bhattacharjee, Electrokinetic Colloid Transport Phenomena, first ed., Wiley, New Jersey, 2006.

[4] F.F. Reuss, Charge-induced flow, Proc. Imperial Soc. Nat. Mosc. 3 (1809) 327–344.

[5] D. Burgreen, F.R. Nakache, Electrokinetic flow in ultrafine capillary slits, J. Phys. Chem. 68 (5) (1964) 1084–1091.

[6] C.L. Rice, R. Whitehead, Electrokinetic flow in a narrow cylindrical capillary, J. Phys. Chem. 69 (11) (1965) 4017–4024.

[7] S. Levine, J.R. Marriott, G. Neale, N. Epstein, Theory of electrokinetic flow in fine cylindrical capillaries at high zeta-potentials, J. Colloid Interface Sci. 52 (1) (1975) 136–149.

[8] Y. Kang, C. Yang, X. Huang, Electroosmotic flow in a capillary annulus with high zeta potentials, J. Colloid Interface Sci. 253 (2) (2002) 285–294.

[9] D. Yang, Analytical solution of mixed electroosmotic and pressure-driven flow in rectangular microchannels, Key Eng. Mater. 483 (2011) 679–683.

[10] C.Y. Wang, Y.H. Liu, C.C. Chang, Analytical solution of electro-osmotic flow in a semicircular microchannel, Phys. Fluids 20 (6) (2008) 063105.

[11] P.F. Eng, P. Nithiarasu, O.J. Guy, An experimental study on an electro-osmotic flow-based silicon heat spreader, Microfluid. Nanofluid. 9 (4–5) (2010) 787–795.

[12] M.F. Al-Rjoub, A.K. Roy, S. Ganguli, R.K. Banerjee, Assessment of an active-cooling micro-channel heat sink device, using electro-osmotic flow, Int. J. Heat Mass Transfer 54 (21–22) (2011) 4560–4569.

[13] D. Maynes, B.W. Webb, Fully developed electro-osmotic heat transfer in microchannels, Int. J. Heat Mass Transfer 46 (8) (2003) 1359–1369.

[14] B.C. Liechty, B.W. Webb, R.D. Maynes, Convective heat transfer characteristics of electro-osmotically generated flow in microtubes at high wall potential, Int. J. Heat Mass Transfer 48 (12) (2005) 2360–2371.

[15] D. Maynes, B.W. Webb, The effect of viscous dissipation in thermally fully-developed electro-osmotic heat transfer in microchannels, Int. J. Heat Mass Transfer 47 (5) (2004) 987–999.

[16] S. Chakraborty, Analytical solutions of Nusselt number for thermally fully developed flow in microtubes under a combined action of electroosmotic forces and imposed pressure gradients, Int. J. Heat Mass Transfer 49 (3–4) (2006) 810–813.

[17] A. Sadeghi, M.H. Saidi, Viscous dissipation effects on thermal transport characteristics of combined pressure and electroosmotically driven flow in microchannels, Int. J. Heat Mass Transfer 53 (19–20) (2010) 3782–3791.

[18] R. Chakraborty, D. Chakraborty, S. Chakraborty, Analytical solution for thermally fully developed combined electroosmotic and pressure-driven flows in narrow confinements with thick electrical double layers, J. Heat Transfer 133 (2) (2011).

[19] A. Garai, S. Chakraborty, Micro-scale thermo-fluidic transport in two immiscible liquid layers subject to combined electroosmotic and pressure-driven transport, Int. J. Heat Mass Transfer 52 (11–12) (2009) 2660–2666.

[20] A. Sadeghi, H. Yavari, M.H. Saidi, S. Chakraborty, Mixed electroosmotically and pressure-driven flow with temperature- dependent properties, J. Thermophys. Heat Transfer 25 (3) (2011) 432–442.

[21] H. Yavari, A. Sadeghi, M.H. Saidi, Hydrodynamic and thermal characteristics of combined electroosmotic and pressure driven flow in a microannulus, J. Heat Transfer 134 (10) (2012) 101703.

[22] L. Graetz, Uber die warmeleitungsfahigheit von flussingkeiten: Part 1, Annalen der Physik und Chemie 252 (1882) 79–94.

[23] L. Graetz, Uber die warmeleitungsfahigheit von flussingkeiten: Part 2, Annalen der Physik und Chemie 261 (1885) 337–357.

[24] J. Lahjomri, A. Oubarra, Analytical solution of the Graetz problem with axial conduction, J. Heat Transfer 121 (4) (1999) 1078–1083.

[25] J. Lahjomri, A. Oubarra, A. Alemany, Heat transfer by laminar Hartmann flow in thermal entrance eregion with a step change in wall temperatures: The Graetz problem extended, Int. J. Heat Mass Transfer 45 (5) (2002) 1127–1148.

[26] A. Haji-Sheikh, J.V. Beck, D.E. Amos, Axial heat conduction effects in the entrance region of parallel plate ducts, Int. J. Heat Mass Transfer 51 (25–26) (2008) 5811–5822.

[27] A. Haji-Sheikh, J.V. Beck, D.E. Amos, Axial heat conduction effects in the entrance region of circular ducts, Heat Mass Transfer 45 (3) (2009) 331–341.

[28] A. Haji-Sheikh, Determination of heat transfer in ducts with axial conduction by variational calculus, J. Heat Transfer 131 (9) (2009) 091702.

[29] A. Haji-Sheikh, W.J. Minkowycz, S. Manafzadeh, Axial conduction effect in flow through circular porous passages with prescribed wall heat flux, Heat Mass Transfer 46 (7) (2010) 727–738.

[30] K. Horiuchi, P. Dutta, Joule heating effects in electroosmotically driven microchannel flows, Int. J. Heat Mass Transfer 47 (14–6) (2004) 3085–3095.

[31] K. Horiuchi, P. Dutta, A. Hossain, Joule-heating effects in mixed electro-osmotic and pressure-driven microflows under constant wall heat flux, J. Eng. Math. 54 (2) (2006) 159–180.

[32] P. Dutta, K. Horiuchi, H.M. Yin, Thermal characteristics of mixed electroosmotic and pressure-driven microflows, Comput. Math. Appl. 52 (5) (2006) 651–670.

[33] S.L. Broderick, B.W. Webb, D. Maynes, Thermally developing electro-osmotic convection in microchannels with finite debye-layer thickness, Numer. Heat Transfer. Part A: Appl. 48 (10) (2005) 941–964.

[34] B.D. Iverson, D. Maynes, B.W. Webb, Thermally developing electroosmotic convection in rectangular microchannels with vanishing Debye-layer thickness, J. Thermophys. Heat Transfer 18 (4) (2004) 486–493.

[35] A. Sharma, S. Chakraborty, Semi-analytical solution of the extended Graetz problem for combined electroosmotically and pressure-driven microchannel flows with step-change in wall temperature, Int. J. Heat Mass Transfer 51 (19–20) (2008) 4875–4885.

[36] R. Dey, D. Chakraborty, S. Chakraborty, Extended Graetz problem for combined electroosmotic and pressure-driven flows in narrow confinements with thick electric double layers, Int. J. Heat Mass Transfer 55 (17–18) (2012) 4724–4733.

[37] R. Dey, T. Ghonge, S. Chakraborty, Steric-effect-induced alteration of thermal transport phenomenon for mixed electroosmotic and pressure driven flows through narrow confinements, Int. J. Heat Mass Transfer 56 (1–2) (2013) 251–262.

[38] A. Sadeghi, H. Veisi, M.H. Saidi, S. Chakraborty, Graetz problem extended to mixed electroosmotically and pressure-driven flow, J. Thermophys. Heat Transfer 26 (1) (2012) 123–133.

[39] X.Y. Chen, K.C. Toh, J.C. Chai, C. Yang, Developing pressure-driven liquid flow in microchannels under the electrokinetic effect, Int. J. Eng. Sci. 42 (5–6) (2004) 609–622.

[40] H.A. Stone, A.D. Stroock, A. Ajdari, Engineering flows in small devices: Microfluidics toward a lab-on-a-chip, Ann. Rev. Fluid Mech. 36 (2004) 381–411.

[41] H.M. Park, J.S. Lee, T.W. Kim, Comparison of the Nernst-Planck model and the Poisson–Boltzmann model for electroosmotic flows in microchannels, J. Colloid Interface Sci. 315 (2) (2007) 731–739.

[42] C. Yang, D. Li, J.H. Masliyah, Modeling forced liquid convection in rectangular microchannels with electrokinetic effects, Int. J. Heat Mass Transfer 41 (24) (1998) 4229–4249.